

# A New Constitutive Model for Thermal Deformation of Magnesium Alloys



JIAN ZENG, FENGHUA WANG, XIAOXIAO WEI, SHUAI DONG,  
ZHENYAN ZHANG, and JIE DONG

Based on the stress–strain curves of as cast Mg-8Gd-3Y alloy, which were obtained by isothermal compression tests at temperatures ranging from 350 °C to 450 °C and strain rates from 0.001 to 1.5 s<sup>-1</sup>, a new constitutive model for thermal deformation of magnesium alloys was proposed from the functional relationship between the ratio of instantaneous stress to peak stress ( $\sigma/\sigma_p$ ) and that of instantaneous strain to peak strain ( $\varepsilon/\varepsilon_p$ ). The undetermined parameters of the model were calculated through parameter regression, and the predicted results agree well with the experimental results. To study the applicability and accuracy of the new model, the stress–strain curves of the compression tests of AZ31B and ZK60 alloys in the literature were modeled and calculated by parameter regression, and their predicted values are very close to the experimental values. Then, the new constitutive model was integrated into a finite element software to simulate the load–stroke curves of isothermal upsetting of the specimen with variable cross-section and plane strain forging of Mg-8Gd-3Y alloy. Under six different process parameters, the simulated load–stroke curves are well consistent with the experimental curves. All the results verify the accuracy of the new model for thermal deformation of magnesium alloys.

<https://doi.org/10.1007/s11661-019-05528-y>

© The Minerals, Metals & Materials Society and ASM International 2019

## I. INTRODUCTION

MAGNESIUM (Mg) alloys have a series of advantages such as high specific strength and stiffness, superior damping performance and electromagnetic shielding characteristics, and can be potentially and widely used in automotive, aerospace, and electron industries.<sup>[1–4]</sup> Unfortunately, because of the hexagonal close-packed crystal structure with limited number of slip systems, Mg alloys have poor formability at room temperature.<sup>[5–7]</sup> Consequently, Mg alloys are usually formed at high temperatures. However, the narrow forming temperature range and high sensitivity to process parameters severely limit the further promotion of Mg alloys. With the help of FE simulation technology, the law of metal flow and the field distributions of strain, stress, and temperature at different deformation times can be predicted, which can provide theoretical guidelines for acquiring the optimal forming

parameters.<sup>[8–10]</sup> Nevertheless, the results of FE simulation can be really credible only when the accuracy of the input constitutive model is high enough.<sup>[11]</sup>

Therefore, many scholars have done lots of work on developing a reasonable constitutive model for thermal deformation of Mg alloys. In the commercial brand Mg alloys, Zhou *et al.*<sup>[12]</sup> developed a new constitutive model of AZ61 alloy and obtained the optimized extrusion temperature and speed. Cai *et al.*<sup>[13]</sup> proposed a constitutive model of AZ41M alloy considering the compensation of strain. Tsao *et al.*<sup>[14]</sup> analyzed the effects of deformation temperature, strain rate, and strain on the flow stress of AZ61 alloy and developed a mathematical model as a function of temperature, strain rate, and strain using the amended Fields–Bachofen equation. Except for the commercial AZ61 and AZ41M alloys, the extensive attention also has been paid to constructing a constitutive model describing the deformation behavior of the other brand alloys, including AZ31,<sup>[15–17]</sup> AZ80,<sup>[18–20]</sup> AZ91,<sup>[21,22]</sup> and ZK60.<sup>[23]</sup> In the study on the constitutive model of rare-earth Mg alloy, Li and Zhang<sup>[24]</sup> investigated the hot deformation behavior of Mg-9Gd-4Y-0.6Zr alloy and constructed a plastic flow semi-empirical model for the relation between strain rate, strain, and temperature. Zhou *et al.*<sup>[25]</sup> used the improved Arrhenius-type equation to predict the flow behavior of the Mg-Gd-Y-Nb-Zr alloy. Using the new fitting method of Rieiro, Carsi, and

---

JIAN ZENG, FENGHUA WANG, XIAOXIAO WEI, SHUAI DONG, ZHENYAN ZHANG, and JIE DONG are with the National Engineering Research Center of Light Alloy Net Forming and State Key Laboratory of Metal Matrix Composite, School of Materials Science and Engineering, Shanghai Jiao Tong University, Shanghai, 200240, P.R. China. Contact e-mail: wangfenghua@sjtu.edu.cn

Manuscript submitted June 29, 2019.

Article published online November 7, 2019

Ruano for direct calculation of the Garofalo constants, the deformation behavior of fine-grained extruded GWK940, GWK540, and GK50 alloys can be described by the Garofalo equation.<sup>[26]</sup> Additionally, Hao *et al.*<sup>[27]</sup> investigated the flow behavior of Mg-Zn-Y-Mn alloy and developed a constitutive equation. The flow stress predicted by the equation agrees well with experimental stress.

In general, the slip systems of the basal, prismatic, and pyramidal plane can be activated when Mg alloys are deformed at high temperatures,<sup>[13,14]</sup> and the effects of original texture and twins on the flow stress at high temperatures are far less intense than that at low temperatures. Therefore, these constitutive models in the current documents all belong to the macroscopic constitutive model, which reflects the change of flow stress with temperature, strain rate, and even strain and does not introduce the effects of original texture and microscopic deformation mechanism on flow stress. Additionally, it can be found that the constitutive model can be mainly classified into three categories. The first one is Arrhenius hyperbolic-type equation,<sup>[16–18,20,24,26–28]</sup> in which the peak stress is used as the flow stress to build the constitutive model. This model does not take strain into account, so it cannot reflect the change of flow stress with strain except for predicting the maximum load during plastic deformation. In recent years, based on the Arrhenius-type equation, the effect of strain was introduced by assuming that different material constants were polynomial functions of strain.<sup>[8,13,19,21–23,25,29]</sup> Then the Arrhenius model considering the strain can give the change law of stress with strain during the entire deformation. However, there are many parameters during the polynomial fitting process, and the slight change of strain will cause a huge fluctuation of stress, which will lead to a large error. The second one is exponential model.<sup>[8,12,15,30,31]</sup> Although the strain is considered, the prediction accuracy is low. The third one is a two-stage model which is based on the work hardening-dynamic recovery and dynamic recrystallization.<sup>[8,32–36]</sup> This model also contains the impact of strain, but the undetermined parameters are numerous, thus the solution process is complicated. Except for the above three categories, by analyzing the relationship between stress and strain, Liu *et al.*<sup>[37]</sup> proposed a new constitutive model with few parameters, and successfully assessed the variation of the flow stress of AZ31B alloy. However, in their subsequent study of AZ61 alloy,<sup>[38]</sup> the authors found that the predicted stress by using this model cannot maintain steady state and increases slightly when the strain is large, implying that this model is not highly accurate.

In this paper, the stress–strain curves of Mg-8Gd-3Y (GW83) alloy were obtained by the isothermal compression experiments. Firstly, starting from the relationship between the ratio of  $\sigma/\sigma_p$  and that of  $\varepsilon/\varepsilon_p$ , a new constitutive model for thermal deformation of Mg alloys was constructed by parameter regression. Subsequently, the adaptability of the new model was investigated by the hot compression stress–strain curves of other Mg alloys in the literature. Finally, the accuracy of the new

model was verified by the comparisons of simulated results and experimental results of isothermal upsetting and plane strain forging (PSF) of GW83 alloy under different process parameters.

## II. MATERIALS AND METHODS

The semi-continuous direct chilling cast ingot of GW83 alloy with a diameter of 300 mm was used in this work, and its chemical composition is Mg-8Gd-3Y (in wt pct). Before the experiment, it has been homogenized at 500 °C for 10 hours.

Firstly, the cylindrical compression specimens with a diameter of 8 mm and height of 12 mm were machined from the homogenized ingot. The hot compression tests were conducted on an Instron 5982 testing machine with an environmental chamber. The compression parameters are as follows: the temperatures of 350 °C, 400 °C, and 450 °C; the strain rates of 0.001, 0.01, 0.1, 0.5, 1, and 1.5 s<sup>-1</sup>; and the total true strain of 1.0. Prior to compression, the top and bottom surfaces of each specimen were coated with graphite to minimize the friction. The specimens were heated to the desired deformation temperatures and held for 5 minutes before hot compression. In the process of hot compression, stress and strain were collected automatically through the processing system of the testing machine. Based on the stress–strain curves under different deformation conditions, the constitutive model for thermal deformation can be established.

By the secondary development using Fortran language, the constitutive model can be coupled to the DEFORM-3D for predicting the load variation during the upsetting and PSF processes. The schematic illustration of the FE model for upsetting specimen with variable cross-section (VCS) is presented in Figure 1(a). The specimen is 16 mm in height. The compressive load was applied along the height direction (Z-axis), and the maximum strain is 1. The schematic illustration of the FE model for PSF is shown in Figure 1(b), and the cuboid specimen for the PSF experiment is 8 mm in length, 10 mm in width, and 10 mm in height. The compression load was applied along the height direction (Z-axis). No constraint occurred in the length direction (X-axis), while the deformation in the width direction (Y-axis) was restricted. The maximum strains in the height and width directions were 1.0 and 0, respectively. During simulation, the workpiece, dies, and ambient air have the same temperature, and the coulomb friction coefficient is 0.20. The dies have greater rigidity and are considered as rigid bodies. Only the deformation of the billet is plastic.<sup>[39]</sup> The heat transfer coefficient between sample and air is 20 N/(s m °C), and that between sample and dies is 11,000 N/(s m °C). The billets are divided *via* the absolute grid method, the mesh type is tetrahedral mesh, and the minimum and maximum mesh sizes are set to 0.25 and 0.50 mm, respectively.

Finally, the cast rod was machined to the specimens for upsetting and PSF experiments along the length direction. The same deformation conditions as the simulation parameters were selected, and the

experiments were performed on the INSTRON5982 test machine with the environmental chamber. Before deformation, graphite was used to reduce the friction at the surfaces between the sample and the dies. The specimens were first heated to the forming temperature and held isothermally for 6 minutes to ensure the uniform temperature. During the forming process, some experimental values were recorded entirely by the processing system on the testing machine.

### III. RESULTS AND DISCUSSION

#### A. True Stress–Strain Curves of GW83 Alloy

Figure 2 shows the true stress–strain curves of GW83 alloy at different conditions. According to Figure 2, the flow stress characteristics can be concluded as follows:

- (1) At the beginning of deformation, due to the leading role of work hardening, the stress increases rapidly to a peak value.<sup>[13,25]</sup>
- (2) When the deformation exceeds the peak strain, the flow stress decreases with increasing strain as softening behavior caused by dynamic recrystallization overtakes work hardening.<sup>[27,37]</sup>
- (3) Deformation temperature and strain rate have a remarkable effect on the flow stress. With the increase of strain rate or the decrease of temperature, the flow stress increases significantly.
- (4) When the temperature is below 400 °C and strain rate is above 0.01 s<sup>-1</sup>, as the time proceeds, the stresses will drop dramatically. It can be noted from Figure 2(f) that the strain-to-failure at the temperature of 350 °C and strain rate of 1.5 s<sup>-1</sup> reaches only 0.23. This is due to the result of the

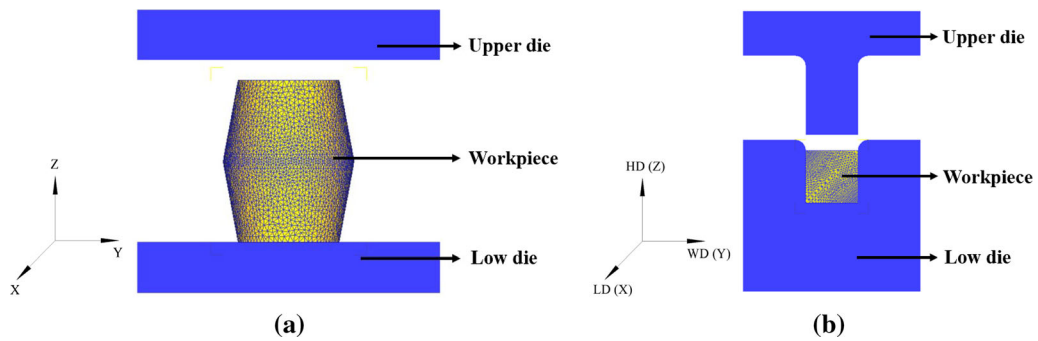


Fig. 1—Schematic illustration of the FE models for: (a) upsetting and (b) PSF.

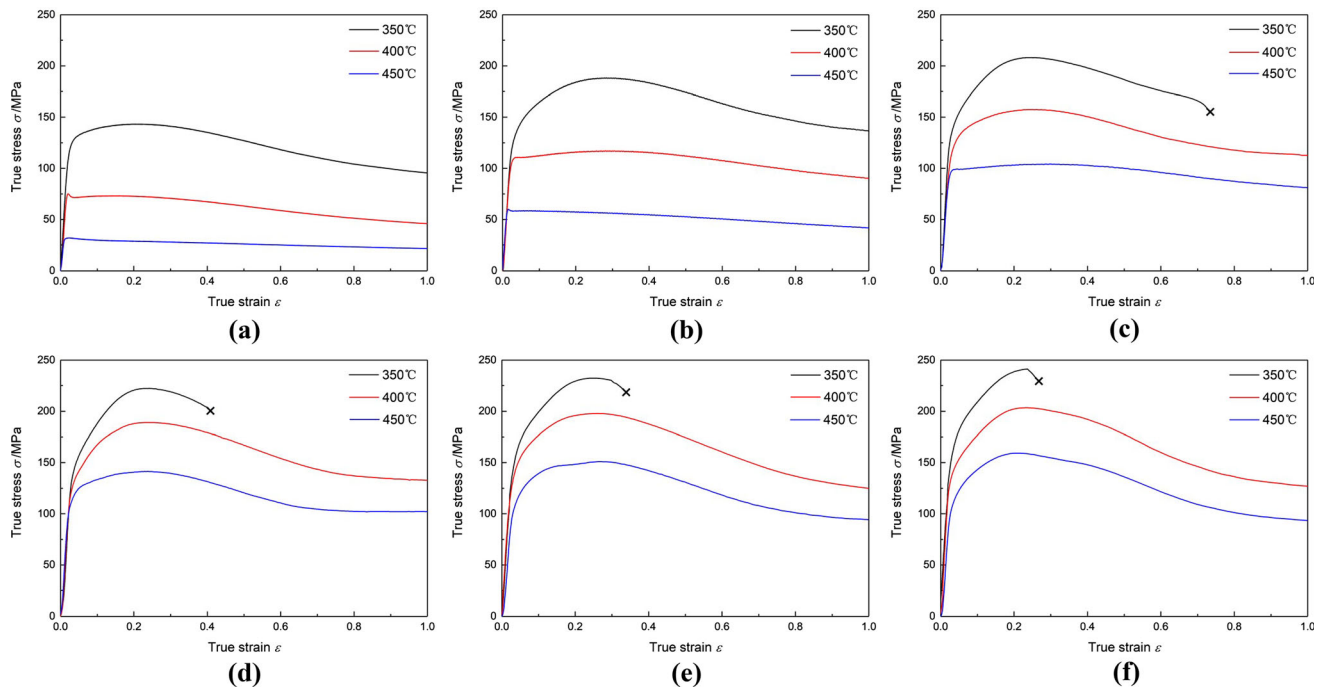


Fig. 2—True stress–strain curves of GW83 alloy at (a)  $\dot{\epsilon} = 0.001 \text{ s}^{-1}$ , (b)  $\dot{\epsilon} = 0.01 \text{ s}^{-1}$ , (c)  $\dot{\epsilon} = 0.1 \text{ s}^{-1}$ , (d)  $\dot{\epsilon} = 0.5 \text{ s}^{-1}$ , (e)  $\dot{\epsilon} = 1 \text{ s}^{-1}$ , and (f)  $\dot{\epsilon} = 1.5 \text{ s}^{-1}$ .

occurrence of premature fracture, which are consistent with the macro-observations.<sup>[24]</sup>

## B. New Constitutive Model

### 1. Proposal of a new constitutive model

The hardening and softening effects of the material during thermal deformation can be well reflected by the ratio of instantaneous stress to peak stress ( $\sigma/\sigma_p$ ). When the value of  $\sigma/\sigma_p$  is 1, the hardening effect caused by work hardening is roughly equal to the softening effect caused by dynamic recrystallization. As strain continues increasing, the softening effect is greater than the hardening effect, that is,  $\sigma/\sigma_p$  is less than 1. Additionally, the ratio of instantaneous strain to peak strain ( $\varepsilon/\varepsilon_p$ ) also reveals the hardening and softening processes of the material. Therefore, it can be guessed that there exists a certain functional relationship between the stress ratio  $\sigma/\sigma_p$  and the strain ratio  $\varepsilon/\varepsilon_p$ , which can be expressed as

$$\frac{\sigma}{\sigma_p} = f\left(\omega \frac{\varepsilon}{\varepsilon_p}\right), \quad [1]$$

where  $\sigma/\sigma_p$  is the stress coefficient,  $\varepsilon/\varepsilon_p$  is the strain coefficient, and  $\omega$  is the undetermined constant of the strain coefficient.

Figure 3 is the stress coefficient–strain coefficient curves under different deformation conditions. It can be found that these curves exhibit approximately exponential relationship both before and after the peak stress. Therefore, Eq. [1] can be further assumed as

$$\frac{\sigma}{\sigma_p} = \left(\omega \frac{\varepsilon}{\varepsilon_p}\right)^{f\left(\frac{\varepsilon}{\varepsilon_p}\right)}. \quad [2]$$

By taking logarithms on both sides of Eq. [2], Eq. [2] can be written as

$$\ln\left(\frac{\sigma}{\sigma_p}\right) = f\left(\frac{\varepsilon}{\varepsilon_p}\right) \cdot \ln\left(\omega \frac{\varepsilon}{\varepsilon_p}\right). \quad [3]$$

Equation [3] can also be presented as

$$f\left(\frac{\varepsilon}{\varepsilon_p}\right) = \frac{\ln\left(\frac{\sigma}{\sigma_p}\right)}{\ln\left(\omega \frac{\varepsilon}{\varepsilon_p}\right)}. \quad [4]$$

The right side of the above equation actually represents the hardening and softening effects of the material, and can be named as “hardening and softening factor”:

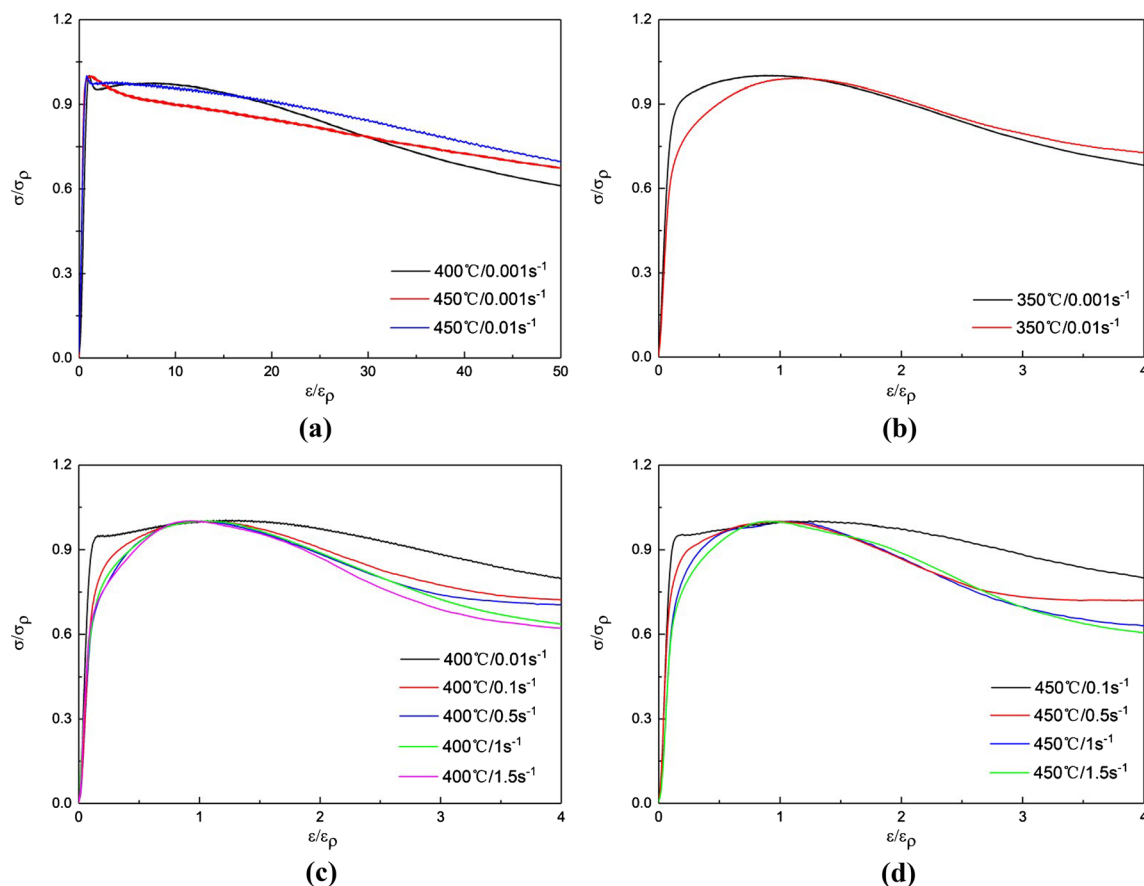


Fig. 3—Relationships between  $\sigma/\sigma_p$  and  $\varepsilon/\varepsilon_p$ : (a) at three conditions of  $\varepsilon_p = 0.02$  and the other conditions: (b)  $T = 350^\circ\text{C}$ , (c)  $T = 400^\circ\text{C}$ , and (d)  $T = 450^\circ\text{C}$ .

$$\theta' = \frac{\ln\left(\frac{\sigma}{\sigma_p}\right)}{\ln\left(\omega \frac{\dot{\varepsilon}}{\dot{\varepsilon}_p}\right)}. \quad [5]$$

To determine the mathematical expression of  $f\left(\frac{\dot{\varepsilon}}{\dot{\varepsilon}_p}\right)$ , the curves of hardening and softening factor and strain coefficient are plotted, as shown in Figure 4. It can be seen that these curves at different deformation temperatures and strain rates exhibit the quadratic functional relationship.

Therefore, the relation between  $\theta'$  and  $\varepsilon/\varepsilon_p$  can be expressed as

$$\theta' = a\left(\frac{\varepsilon}{\varepsilon_p} + b\right)^2 + c, \quad [6]$$

where  $a$ ,  $b$  and  $c$  are constants.

Observing Eq. [6], when  $\varepsilon/\varepsilon_p$  equals 1 or  $\sigma/\sigma_p$  equals 1, the hardening and softening effects achieve balance, and the values of  $\theta'$  are equal to 0 at this time. To make Eq. [6] rational under any conditions, we assume the values of  $b$  and  $c$  equal  $-1$  and  $0$ , respectively. For the purpose of checking the universality of the equations ( $b = -1$  and  $c = 0$ ), the curves in Figure 4 are fitted by least square method, and the values of parameter  $b$

and  $c$  under different conditions can be calculated, as listed in Table I.

It can be observed from Table I that the values of  $b$  and  $c$  under different deformation conditions are

**Table I. Values of  $b$  and  $c$  at Different Conditions**

Strain Rate ( $s^{-1}$ )	Temperature ( $^{\circ}C$ )		
	350	400	450
0.001	$b$ $-0.926$	$-1.020$	$-1.086$
	$c$ $-0.00412$	$0.00637$	$0.0347$
0.01	$b$ $-1.113$	$-1.093$	$-0.916$
	$c$ $0.00481$	$-0.00101$	$0.00995$
0.1	$b$ —	$-0.914$	$-1.135$
	$c$ —	$0.00539$	$-0.0191$
0.5	$b$ —	$-0.936$	$-1.025$
	$c$ —	$0.01294$	$0.00265$
1.0	$b$ —	$-0.908$	$-0.954$
	$c$ —	$0.0865$	$0.00297$
1.5	$b$ —	$-1.001$	$-1.042$
	$c$ —	$-0.000867$	$-0.00294$

“—” means that the specimen cracks under the deformation condition.

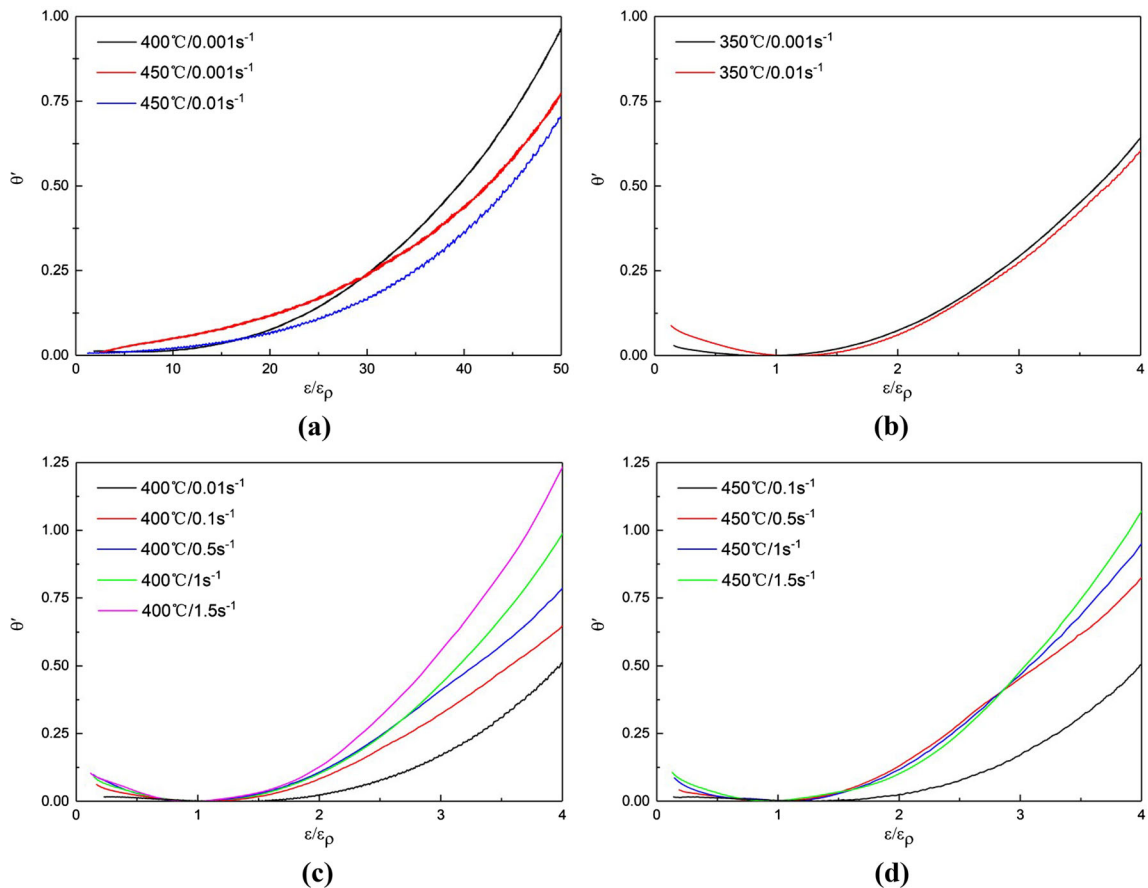


Fig. 4—Relationships between  $\theta'$  and  $\varepsilon/\varepsilon_p$ : (a) at three conditions of  $\varepsilon_p = 0.02$  and the other conditions: (b)  $T = 350^{\circ}C$ , (c)  $T = 400^{\circ}C$ , and (d)  $T = 450^{\circ}C$ .

approximately equal to about  $-1$  and  $0$ , respectively. Thus, Eq. [6] can be written as

$$\theta' = \frac{\ln\left(\frac{\sigma}{\sigma_p}\right)}{\ln\left(\omega \frac{\varepsilon}{\varepsilon_p}\right)} = a \left(\frac{\varepsilon}{\varepsilon_p} - 1\right)^2. \quad [7]$$

Based on Eq. [7], the new constitutive model can be built and expressed as

$$\sigma = \sigma_p \cdot \left(\omega \frac{\varepsilon}{\varepsilon_p}\right)^a \left(\frac{\varepsilon}{\varepsilon_p} - 1\right)^2. \quad [8]$$

In this constitutive model, the peak stress and peak strain are read from the experimental data in Figure 2. The values of  $a$  and  $\omega$  at different conditions are presented in Table II which are obtained by fitting the stress-strain curves at different temperatures and strain rates in Figure 2 using least square method.

Table III displays the ratios of the value of  $\omega$  to the corresponding peak strain at different conditions. It can be recognized that the value of  $\omega/\varepsilon_p$  has always been maintained about  $0.6$ . Thus, Eq. [8] can be simplified as

$$\sigma = \sigma_p \cdot (0.6\varepsilon)^a \left(\frac{\varepsilon}{\varepsilon_p} - 1\right)^2. \quad [9]$$

For the convenience of calculation, Eq. [9] can be further simplified as

$$\sigma = \sigma_p \cdot (0.6\varepsilon)^\varphi (\varepsilon - \varepsilon_p)^2, \quad [10]$$

where  $\varphi$  is the modified parameter related to the hardening and softening effects.

The peak stress and peak strain in the new model can be determined based on the Arrhenius-type equation and Zener-Hollomon parameter ( $Z$ ).<sup>[8,37]</sup>

**Table II. Values of  $a$  and  $\omega$  at Different Conditions**

Strain Rate ( $s^{-1}$ )	Temperature ( $^{\circ}C$ )			
	350	400	450	
0.001	$a$	0.0783	3.315E-4	3.892E-4
	$\omega$	0.141	0.0125	0.0133
0.01	$a$	0.105	0.0504	1.384E-4
	$\omega$	0.166	0.134	0.00104
0.1	$a$	—	0.0910	0.0844
	$\omega$	—	0.148	0.136
0.5	$a$	—	0.131	0.109
	$\omega$	—	0.151	0.145
1.0	$a$	—	0.152	0.186
	$\omega$	—	0.150	0.149
1.5	$a$	—	0.172	0.202
	$\omega$	—	0.156	0.139

“—” Means that the specimen cracks under the deformation condition.

## 2. Calculations of $\sigma_p$ and $\varepsilon_p$

Arrhenius equation has been widely used to describe the relationship among flow stress, deformation temperature, and strain rate during isothermal compression,<sup>[27,40,41]</sup> as listed in Eq. [11]. Meanwhile, the comprehensive effects of temperature and strain rate on the deformation behavior of alloys can also be expressed by  $Z$  parameter, as shown in Eq. [12].

$$\dot{\varepsilon} = A(\sinh(\alpha\sigma))^n \exp\left(-\frac{Q}{RT}\right), \quad [11]$$

$$Z = \dot{\varepsilon} \exp\left(\frac{Q}{RT}\right), \quad [12]$$

where  $\dot{\varepsilon}$  is strain rate;  $Q$  is the activation energy ( $\text{kJ mol}^{-1}$ );  $R$  is universal gas constant ( $8.314 \text{ J mol}^{-1} \text{ K}^{-1}$ );  $T$  is temperature ( $\text{K}$ );  $A$ ,  $A_1$ ,  $A_2$ ,  $\alpha$ ,  $n$ ,  $\beta$  are the material constants,  $\alpha = \beta/n_1$ ; and  $\sigma$  is true stress ( $\text{MPa}$ ).

In addition to Eq. [11], two other equations are usually adopted to describe the relationship of the flow stress with the temperature and strain rate. For the case of low stress level, the equation can be expressed as Eq. [13], while Eq. [14] is suitable for expression of high stress level.

$$\dot{\varepsilon} = A_1 \sigma^{n_1}, \quad [13]$$

$$\dot{\varepsilon} = A_2 \exp(\beta\sigma). \quad [14]$$

Taking the logarithm of both sides of Eqs. [13] and [14], then gives

$$\ln \dot{\varepsilon} = \ln A_1 + n_1 \ln \sigma \quad [15]$$

$$\ln \dot{\varepsilon} = \ln A_2 + \beta\sigma. \quad [16]$$

In general, the material has no enough time for the heat exchange when deformed at high strain rates. The adiabatic temperature rise at high strain rates is more serious than that at low strain rates, which results in a remarkable softening effect at high strain rates.<sup>[35,42,43]</sup> After the peak stress, with the increase of strain, the stress at high strain rates ( $> 0.1 \text{ s}^{-1}$ ) decreases faster than that at low strain rates ( $\leq 0.1 \text{ s}^{-1}$ ) at the same temperature, as shown in Figure 2. That is, the softening effect of GW83 alloy at high strain rates is more significant. Therefore, in order to acquire more precise results, the expressions of peak stress and peak strain of GW83 alloy at low strain rates ( $\leq 0.1 \text{ s}^{-1}$ ) and high strain rates ( $> 0.1 \text{ s}^{-1}$ ) should be computed, respectively.

Substituting the peak stress and corresponding strain rate at low strain rates ( $\leq 0.1 \text{ s}^{-1}$ ) into Eqs. [15] and [16], the corresponding relationships of some parameters can be clearly reflected in Figures 5(a) and (b). By using the linear regression calculation, the average values of  $n_1$  and  $\beta$  are  $6.008$  and  $0.0629$ , respectively. Then, the value of  $\alpha$  can be easily determined by  $\alpha = \beta/n_1$ , and equals to  $0.0105$ .

To determine the deformation activation energy  $Q$ , the logarithms was taken on both sides of Eq. [11], so Eq. [11] can be expressed as

$$\ln \dot{\epsilon} = n \cdot \ln[\sinh(\alpha\sigma)] + \ln A - \frac{Q}{RT}. \quad [17]$$

For a given strain rate, differentiating Eq. [17] with respect to  $1/T$ , and the deformation activation energy can be counted by the following relationship:

Strain Rate ( $s^{-1}$ )		Temperature ( $^{\circ}C$ )		
		350	400	450
0.001	$\omega/\epsilon_p$	0.613	0.602	0.591
0.01	$\omega/\epsilon_p$	0.626	0.583	0.609
0.1	$\omega/\epsilon_p$	—	0.617	0.591
0.5	$\omega/\epsilon_p$	—	0.604	0.604
1.0	$\omega/\epsilon_p$	—	0.612	0.573
1.5	$\omega/\epsilon_p$	—	0.624	0.585

$$Q = R \cdot n \cdot w = R \cdot \left[ \frac{\partial \ln \dot{\epsilon}}{\partial \ln(\sinh(\alpha\sigma_p))} \right]_T \cdot \left[ \frac{\partial \ln(\sinh(\alpha\sigma_p))}{\partial (1/T)} \right]_{\dot{\epsilon}}. \quad [18]$$

Substituting the stress–strain data into Eq. [18], the relationships of  $\ln(\sinh(\alpha\sigma_p)) - \ln \dot{\epsilon}$  and  $\ln(\sinh(\alpha\sigma_p)) - 1/T$  can be given, as shown in Figures 5(c) and (d). By linear fitting, the values of  $n$  and  $w$  can be calculated from the average slope of fitting straight lines, and the mean values are evaluated as 3.846 and 6.930, respectively. After calculation, the value of deformation activation energy at low strain rates ( $\leq 0.1 s^{-1}$ ) equals 221.591 KJ/mol. By using the same resolution method, the activation energy at high strain rates ( $> 0.1 s^{-1}$ ) can be calculated to be 248.677 kJ/mol.

After taking the logarithm of both sides of Eq. [12], the relationship between peak stress and  $Z$  parameter can be represented as

$$\ln Z = \ln A + n \ln(\sinh(\alpha\sigma_p)). \quad [19]$$

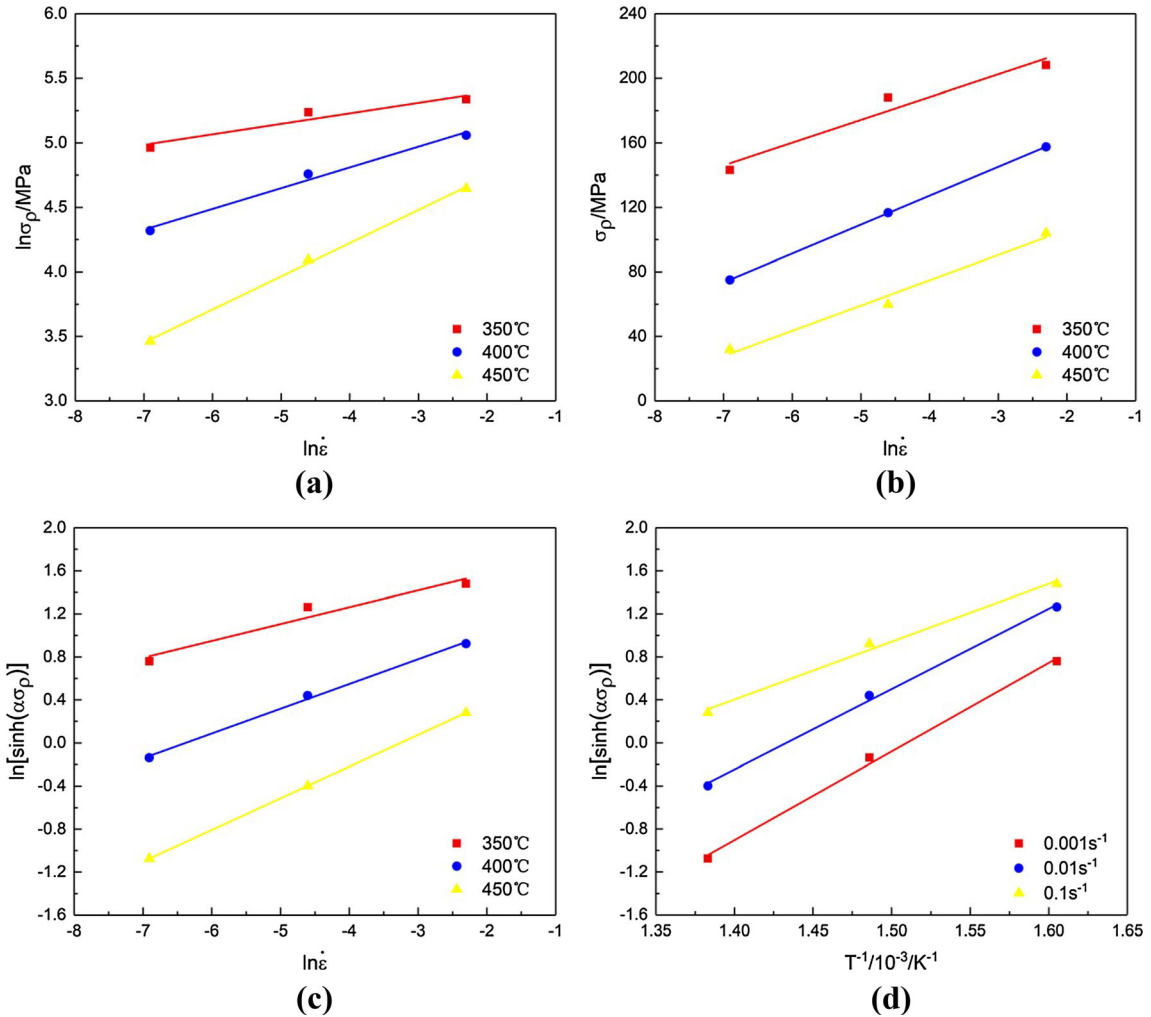


Fig. 5—Relationships between (a)  $\ln \sigma_p$  and  $\ln \dot{\epsilon}$ , (b)  $\sigma_p$  and  $\ln \dot{\epsilon}$ , (c)  $\ln(\sinh(\alpha\sigma_p))$  and  $\ln \dot{\epsilon}$ , and (d)  $\ln(\sinh(\alpha\sigma_p))$  and  $(1/T)$ .

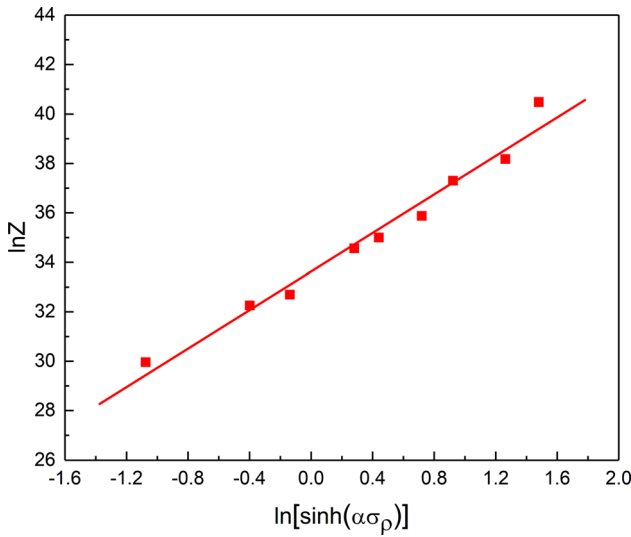


Fig. 6—Relationship between  $\ln Z$  and  $\ln(\sinh(\alpha\sigma_p))$ .

Subsequently, according to Eq. [19], the  $\ln Z - \ln(\sinh(\alpha\sigma_p))$  curve can be obtained, as shown in Figure 6. The values of  $A$  and  $n$  can be evaluated from the slope and intercept of the straight line, respectively.

The logarithm is removed from both sides of Eq. [19] and can be transformed into

$$\left(\frac{Z}{A}\right)^{\frac{1}{n}} = \sinh(\alpha\sigma_p) = \frac{e^{\alpha\sigma_p} - e^{-\alpha\sigma_p}}{2}. \quad [20]$$

Then the peak stress can be written as a function of  $Z$  parameter:

$$\sigma_p = \frac{1}{\alpha} \cdot \ln \left[ \left(\frac{Z}{A}\right)^{\frac{1}{n}} + \left( \left(\frac{Z}{A}\right)^{\frac{2}{n}} + 1 \right)^{\frac{1}{2}} \right], \quad [21]$$

where at low strain rates ( $\leq 0.1 \text{ s}^{-1}$ ),  $\alpha$  is 0.0105,  $n$  is 3.899, and  $A$  is  $4.026 \times 10^{14}$ .

Using the same method as above, the parameters at high strain rates ( $> 0.1 \text{ s}^{-1}$ ) can be counted.  $\alpha$  is 0.00613,  $n$  is 8.519, and  $A$  is  $5.018 \times 10^{17}$ .

In addition, the peak strain can also be expressed as a function of  $Z$  parameter, which can be expressed by

$$\varepsilon_p = A_p Z^{n_p}. \quad [22]$$

After taking logarithm on both sides of the above equation, the relationship of  $\ln \varepsilon_p$  and  $\ln Z$  at low strain rates ( $\leq 0.1 \text{ s}^{-1}$ ) can be given, as depicted in Figure 7. It can be concluded that the peak strain at three conditions of  $400 \text{ }^\circ\text{C}/0.001 \text{ s}^{-1}$ ,  $450 \text{ }^\circ\text{C}/0.001 \text{ s}^{-1}$ , and  $450 \text{ }^\circ\text{C}/0.01 \text{ s}^{-1}$  is 0.02. Under the other deformation conditions, the relationship between the peak strain and  $Z$  parameter can be built by parameter fitting:

$$\varepsilon_p = 0.157Z^{0.0112}. \quad [23]$$

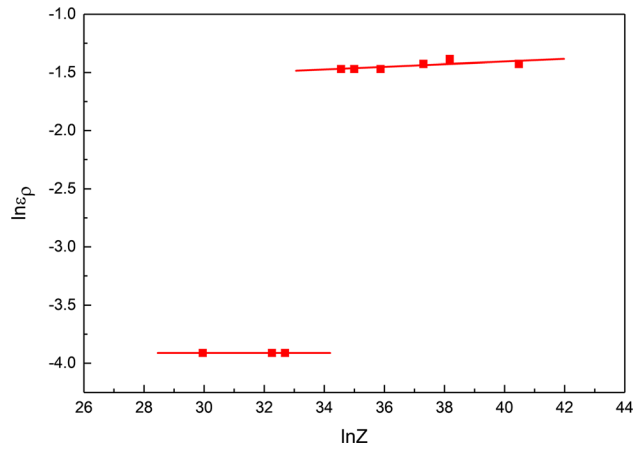


Fig. 7—Relationship between  $\ln \varepsilon_p$  and  $\ln Z$ .

Similarly, the expression of peak strain at high strain rates ( $> 0.1 \text{ s}^{-1}$ ) can be computed:

$$\varepsilon_p = 0.240Z^{0.000558}. \quad [24]$$

### 3. Establishment of new constitutive model of GW83 alloy

According to the solving processes of the peak stress and peak strain mentioned above, both  $\sigma_p$  and  $\varepsilon_p$  depend on the deformation temperature and strain rate. Therefore, the new constitutive model can also be considered as the relationship function between flow stress and deformation temperature, strain rate and strain at any times, reflecting the effects of temperature, strain rate, and strain on flow stress.

In conclusion, the constitutive model for hot deformation of GW83 alloy can be expressed as

$$\sigma = f(\varepsilon, T, \dot{\varepsilon}) = \sigma_p \cdot (0.6\varepsilon)^{\varphi(\varepsilon - \varepsilon_p)^2}, \quad [25]$$

where

$$\sigma_p = \begin{cases} \left\{ 95.238 \cdot \ln \left[ \left(\frac{Z}{4.026 \cdot 10^{14}}\right)^{0.256} + \left(\left(\frac{Z}{4.026 \cdot 10^{14}}\right)^{0.513} + 1\right)^{\frac{1}{2}} \right] \right\} (\dot{\varepsilon} \leq 0.1 \text{ s}^{-1}) \\ \left\{ 163.132 \cdot \ln \left[ \left(\frac{Z}{5.018 \cdot 10^{17}}\right)^{0.117} + \left(\left(\frac{Z}{5.018 \cdot 10^{17}}\right)^{0.23513} + 1\right)^{\frac{1}{2}} \right] \right\} (\dot{\varepsilon} > 0.1 \text{ s}^{-1}) \end{cases}$$

$$\varepsilon_p = \begin{cases} 0.02 (\text{conditions of } 400 \text{ }^\circ\text{C}/0.001 \text{ s}^{-1}, 450 \text{ }^\circ\text{C}/0.001 \text{ s}^{-1} \text{ and } 450 \text{ }^\circ\text{C}/0.01 \text{ s}^{-1}) \\ 0.157Z^{0.0112} (\text{other conditions of } \dot{\varepsilon} \leq 0.1 \text{ s}^{-1}) \\ 0.240Z^{0.000558} (\text{other conditions of } \dot{\varepsilon} > 0.1 \text{ s}^{-1}) \end{cases}$$

$$Z = \begin{cases} \dot{\varepsilon} \exp\left(\frac{26.652.754}{T}\right) (\dot{\varepsilon} \leq 0.1 \text{ s}^{-1}) \\ \dot{\varepsilon} \exp\left(\frac{29.910.633}{T}\right) (\dot{\varepsilon} > 0.1 \text{ s}^{-1}). \end{cases} \quad [26]$$

Subsequently, by combining Eq. [25] with Eq. [26], the stress-strain curves of GW83 alloy under different deformation conditions were fitted through least square method, and multiple sets of  $\varphi$  were counted. The similar values of  $\varphi$  were averaged, and the average was taken as the final result:

$$\varphi = \begin{cases} 0.95 (\dot{\varepsilon} \leq 0.1 \text{ s}^{-1}), \\ 1.63 (\dot{\varepsilon} > 0.1 \text{ s}^{-1}). \end{cases} \quad [27]$$



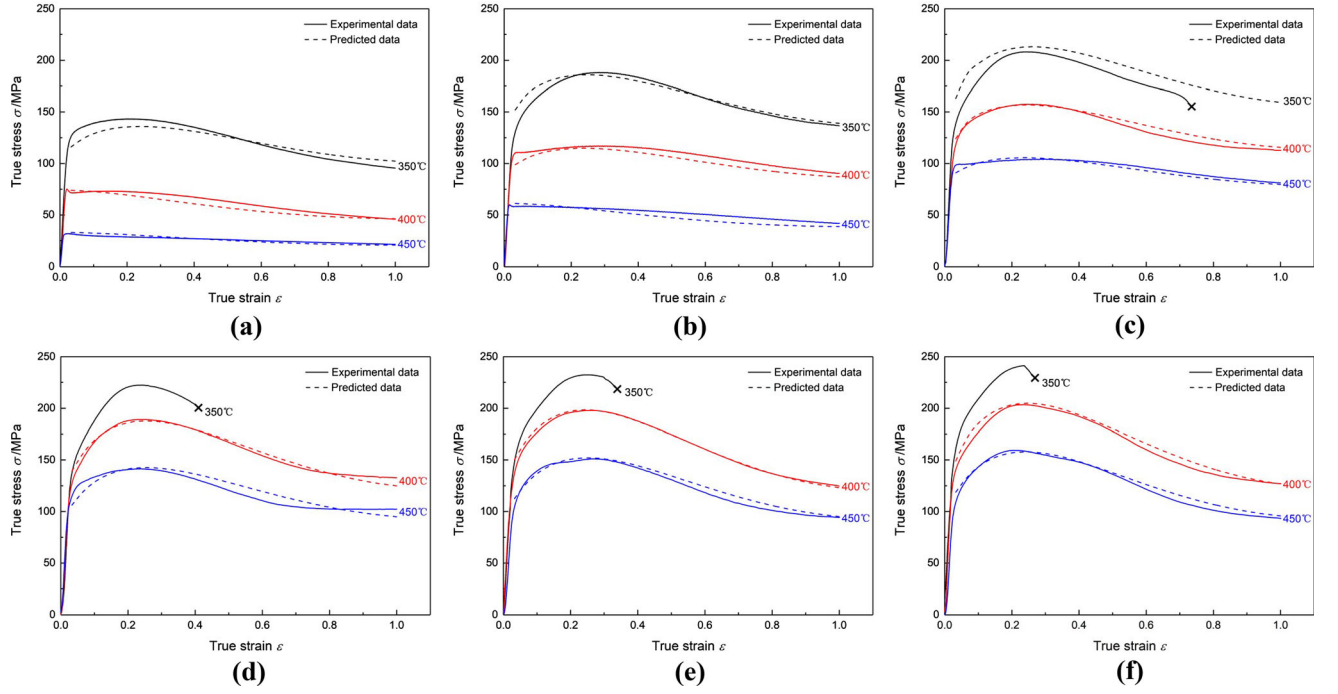


Fig. 8—Comparisons between model prediction values and experimental values of GW83 alloy at (a)  $\dot{\varepsilon} = 0.001 \text{ s}^{-1}$ , (b)  $\dot{\varepsilon} = 0.01 \text{ s}^{-1}$ , (c)  $\dot{\varepsilon} = 0.1 \text{ s}^{-1}$ , (d)  $\dot{\varepsilon} = 0.5 \text{ s}^{-1}$ , (e)  $\dot{\varepsilon} = 1 \text{ s}^{-1}$ , and (f)  $\dot{\varepsilon} = 1.5 \text{ s}^{-1}$ .

Through Eqs. [25], [26], and [27], the predicted values of the new constitutive model of GW83 alloy under different deformation conditions can be given. Figure 8 demonstrates the comparisons between the predicted and experimental results. It is evident that the predicted values have a good agreement with experimental values, which indicates that the new constitutive model can accurately describe the characteristic of flow stress of GW83 alloy.

#### IV. STUDY ON THE APPLICABILITY OF NEW CONSTITUTIVE MODEL

##### A. Applicability of New Constitutive Model in AZ31B Alloy

To study the applicability of the new constitutive model in other Mg alloys, the AZ31B alloy is taken as an example. Based on the stress–strain curves obtained from the literature,<sup>[44]</sup> the constitutive model of AZ31B alloy can be constructed by analyzing and solving according to the above calculation steps:

$$\sigma = \sigma_p \cdot (0.6\varepsilon)^{\varphi_{AZ31B}(\varepsilon - \varepsilon_p)^2}, \quad [28]$$

where

$$\begin{cases} \sigma_p = 88.496 \cdot \ln \left[ \left( \frac{Z}{9.819 \times 10^{11}} \right)^{0.162} + \left( \left( \frac{Z}{9.819 \times 10^{11}} \right)^{0.324} + 1 \right)^{\frac{1}{2}} \right] \\ \varepsilon_p = 0.00753 Z^{0.103} \\ Z = \dot{\varepsilon} \exp \left( \frac{19,092,170}{T} \right) \\ \varphi_{AZ31B} = \begin{cases} 1.28 & (T = 350 \text{ }^\circ\text{C} \text{ and } \dot{\varepsilon} = 1 \text{ s}^{-1} \text{ or } T \leq 300 \text{ }^\circ\text{C}) \\ 0.86 & (\text{other conditions}). \end{cases} \end{cases} \quad [29]$$

By Eqs. [28] and [29], the predicted values of AZ31B alloy under different deformation conditions can be calculated. Figure 9 exhibits the comparisons between the predicted and experimental stresses. It can be found that there exists a good agreement between the predicted and experimental values, suggesting that the new model can be suitable for analyzing the flow characteristics of AZ31B alloy.

##### B. Applicability of New Constitutive Model in ZK60 Alloy

Then taking the ZK60 alloy as an example, based on the experimental results in the literature,<sup>[45]</sup> the constitutive model of ZK60 alloy was established by the above same solution method:

$$\sigma = \sigma_p \cdot (0.6\varepsilon)^{\varphi_{ZK60}(\varepsilon - \varepsilon_p)^2}, \quad [30]$$

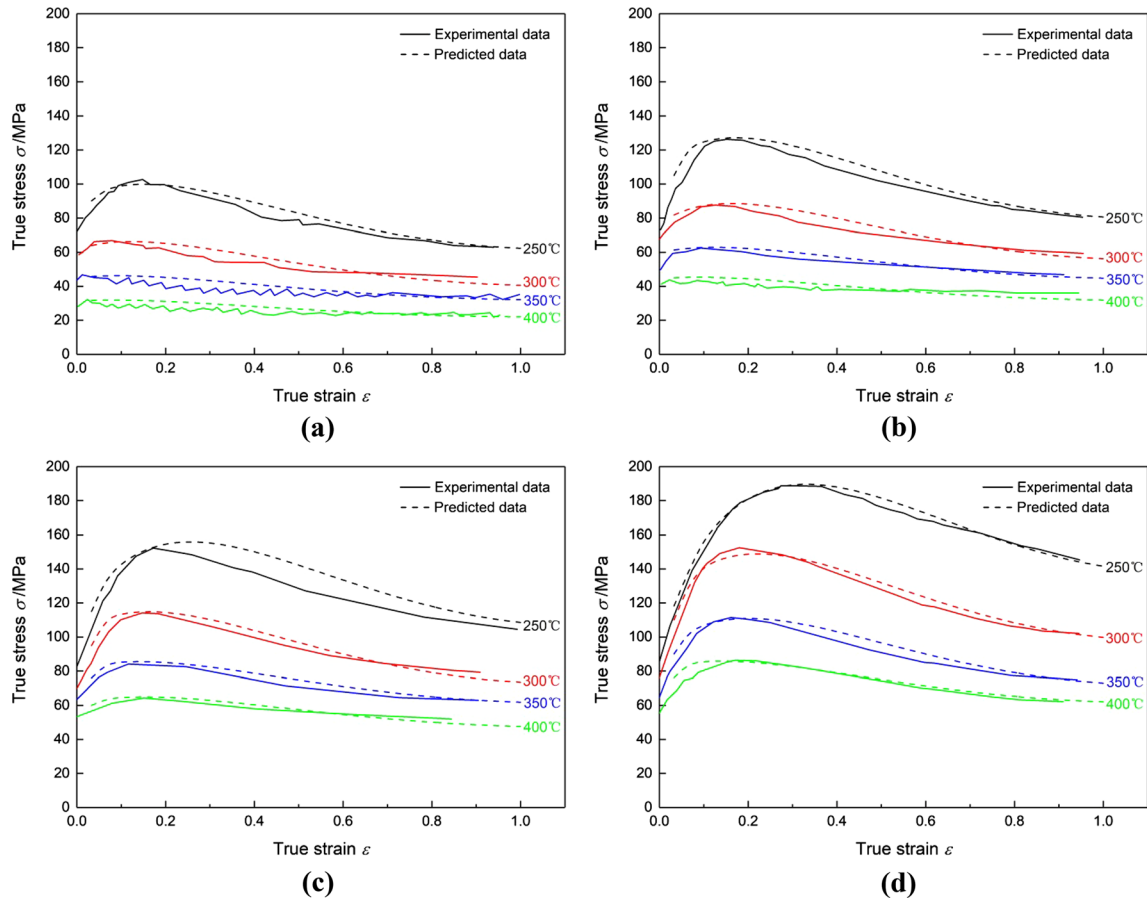


Fig. 9—Comparisons between model prediction values and experimental values of AZ31B alloy at (a)  $\dot{\epsilon} = 0.001 \text{ s}^{-1}$ , (b)  $\dot{\epsilon} = 0.01 \text{ s}^{-1}$ , (c)  $\dot{\epsilon} = 0.1 \text{ s}^{-1}$ , and (d)  $\dot{\epsilon} = 1 \text{ s}^{-1}$ .

where

$$\begin{cases} \sigma_p = 50.505 \cdot \ln \left[ \left( \frac{Z}{5.108 \cdot 10^9} \right)^{0.275} + \left( \left( \frac{Z}{5.108 \cdot 10^9} \right)^{0.550} + 1 \right)^{\frac{1}{2}} \right] \\ \epsilon_p = 0.0242 Z^{0.0328} \\ Z = \dot{\epsilon} \exp \left( \frac{17,003.248}{T} \right) \\ \varphi_{\text{ZK60}} = \begin{cases} 0.99 & (\dot{\epsilon} \leq 0.1 \text{ s}^{-1}) \\ 1.20 & (\dot{\epsilon} > 0.1 \text{ s}^{-1}) \quad (T < 350 \text{ }^\circ\text{C}) \\ 0.67 & (\dot{\epsilon} > 0.1 \text{ s}^{-1}) \quad (T \geq 350 \text{ }^\circ\text{C}). \end{cases} \end{cases} \quad [31]$$

Based on Eqs. [30] and [31], the prediction values of ZK60 alloy at different conditions can be computed. Figure 10 shows a comparison between the predicted and experimental stress–strain curves at different conditions. It can be found that the predicted result of the model is consistent with the experimental result.

Accordingly, it can be concluded that the new constitutive model is suitable not only for GW83 alloy, but also for other Mg alloys such as AZ31B and ZK60. It has good universality for Mg alloys and is a constitutive model for thermal deformation of Mg alloys.

## V. VERIFICATION OF THE ACCURACY OF THE NEW CONSTITUTIVE MODEL

### A. Simulation Prediction and Experimental Verification of Upsetting Specimen with VCS

#### 1. Simulation prediction of upsetting specimen with VCS

The rationality and validity of the new constitutive model depend not only on the accuracy of characterization on flow stress, but also on the reliability and feasibility in FE simulation process. To further investigate the accuracy of the new constitutive model, the constitutive model for hot deformation of GW83 alloy (Eqs. [25],[26] and [27]) is incorporated into the FE software to predict the load variations under different deformation conditions. The specific parameters are listed in Table IV. The first three groups have the same velocity and different temperatures, and the last three groups have different velocities at the same temperature.

Figure 11 shows the specimens after upsetting simulation under different process parameters. All specimens are drum-shaped. With the help of the ruler below Figure 11, it can be measured that the maximum external dimension of these samples is about 20.0 mm.

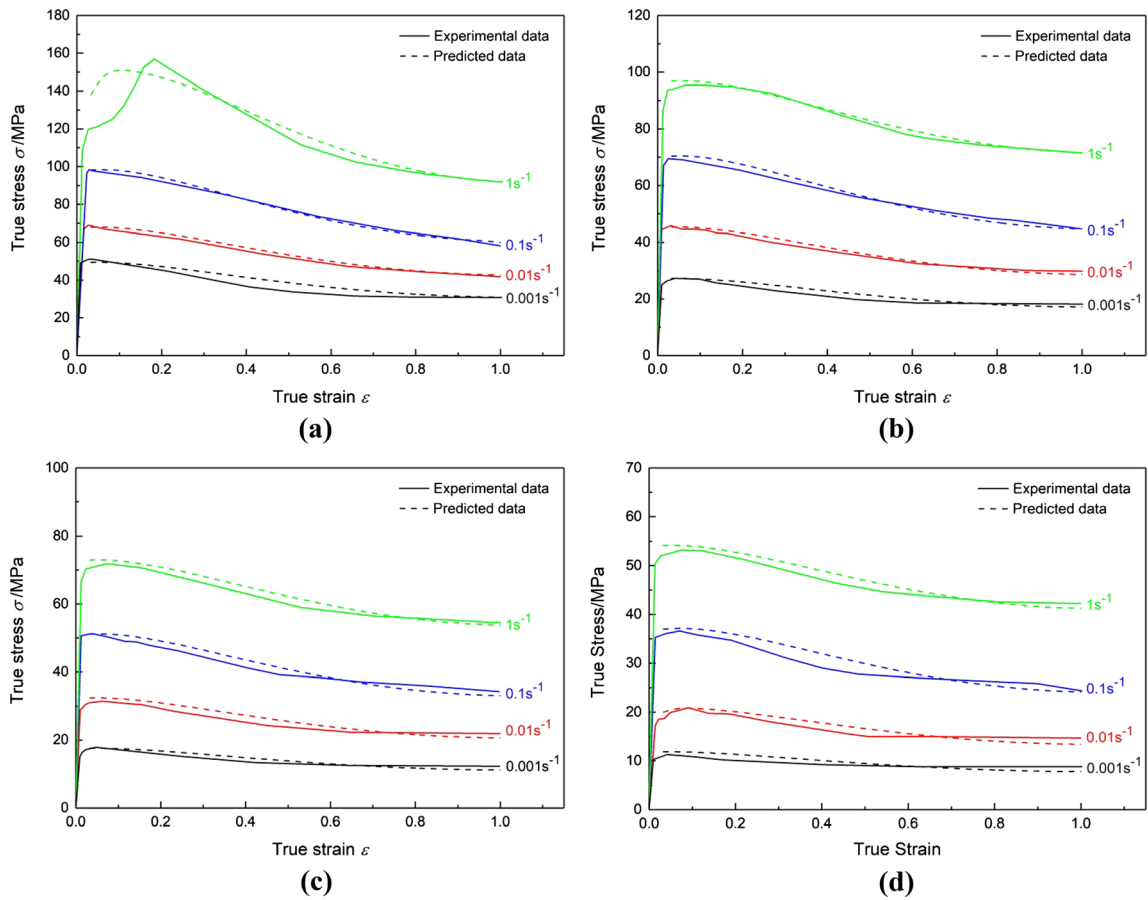


Fig. 10—Comparisons between model prediction values and experimental values of ZK60 alloy at (a)  $T = 300\text{ }^{\circ}\text{C}$ , (b)  $T = 350\text{ }^{\circ}\text{C}$ , (c)  $T = 400\text{ }^{\circ}\text{C}$ , and (d)  $T = 450\text{ }^{\circ}\text{C}$ .

**Table IV. Parameters Used for the Simulation of Upsetting Specimen with VCS**

Number	Temperature ( $^{\circ}\text{C}$ )	Velocity (mm/s)	Stroke (mm)
1	350	0.02	10.12
2	400	0.02	10.12
3	450	0.02	10.12
4	400	0.1	10.12
5	400	0.6	10.12
6	400	3.6	10.12

Then, taking the sample under the fourth parameter as an example, the effective strain distributions of the middle section of the sample at different strokes during the upsetting process were obtained, as shown in Figure 12. Due to the symmetry, only half of the sample was taken for analysis. In the early stage shown in Figure 12(a), the deformation zone mainly focuses on the center area and two diagonal areas, and the contact areas between the billet and dies and the maximum outer edge area of the billet all have a small deformation. With the increase of stroke, the effective strain of each region increases continuously (Figures 12(b) through and (d)). When the stroke reached to 10.12

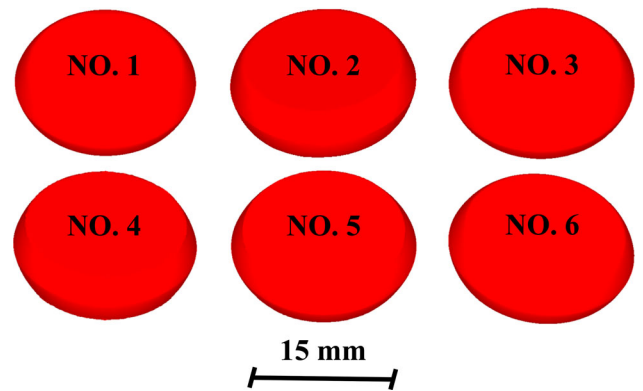


Fig. 11—The specimens after upsetting simulation under different process parameters.

mm (Figure 12(e)), the effective strains at both the center and two diagonal areas exceed 1.0.

The load–stroke curves of upsetting simulation are displayed in Figure 13. At the initial stage, the load increases rapidly due to the work hardening which resulted from the continuous accumulation of dislocations. Subsequently, the load increases slowly and exhibits the characteristic of strain softening, which is a typical phenomenon caused by the dynamic recovery

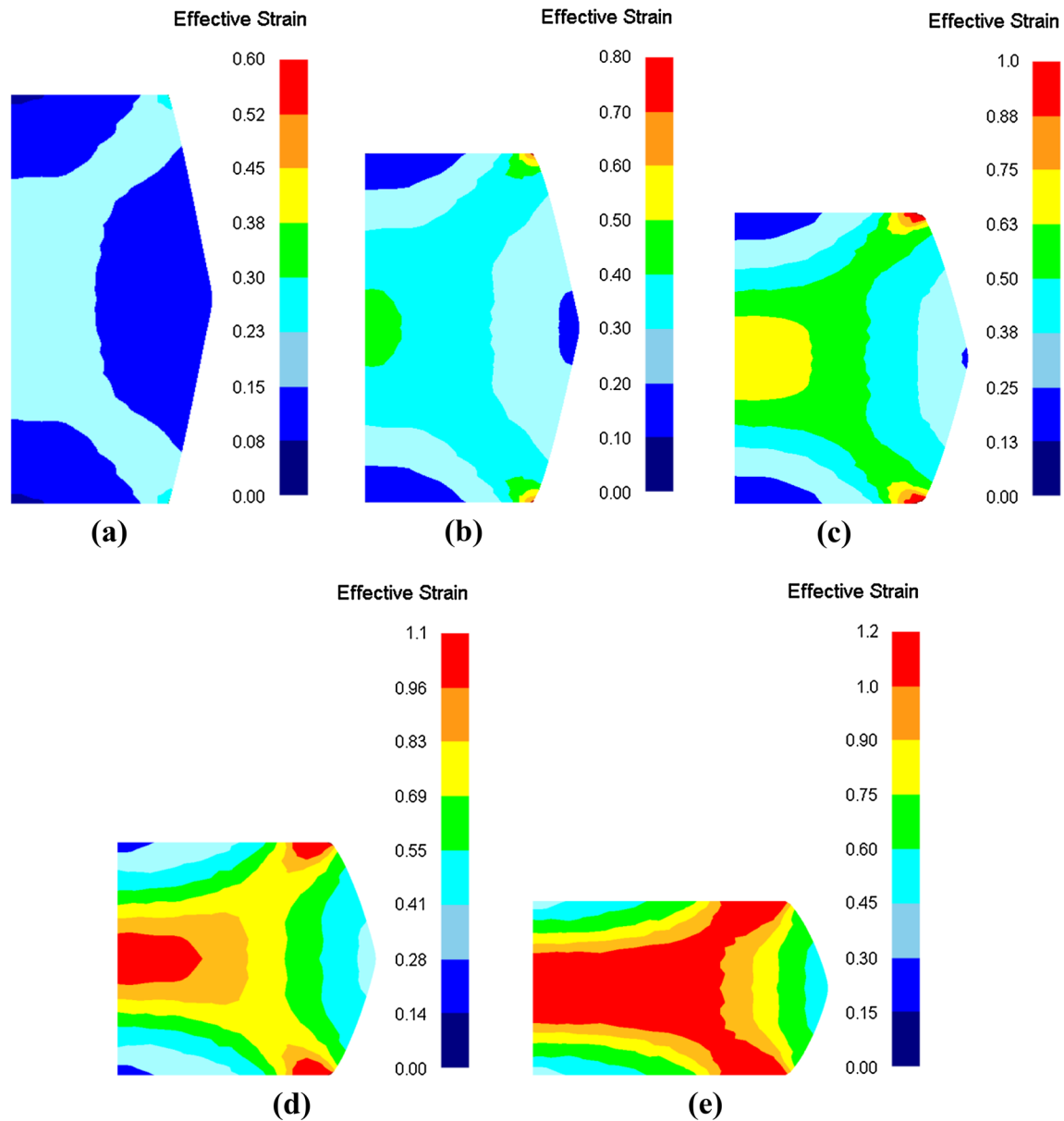


Fig. 12—Distributions of effective strain at different strokes during the upsetting process: (a) 2.024 mm, (b) 4.048 mm, (c) 6.072 mm, (d) 8.096 mm, and (e) 10.12 mm.

or recrystallization.<sup>[46]</sup> The load increases sharply again in the later stage of upsetting, which is the reason that the contact areas between the dies and billet and friction force increase continuously.<sup>[39]</sup> Additionally, it can be found from Figure 13 that the load decreases with increasing temperature at a given velocity and increases with increasing velocity at a given temperature. This can be attributed to the fact that higher temperature can offer higher mobility at grain boundaries for the nucleation and growth of dynamically recrystallized grains while lower velocity can provide sufficient time for energy accumulation and dislocation annihilation.<sup>[40,47]</sup>

## 2. Experimental verification of upsetting specimen with VCS

To verify the reliability of the simulation results, using the same deformation conditions as the simulated parameters, the experiments of the isothermal upsetting specimen with VCS were carried out. As depicted in Figure 14, no macro-cracks appear on the surfaces of the deformed specimens, and the specimens are also drum-shaped. The measured shape size, which is basically the same and approximately equal to 20 mm, agrees with that of the simulated specimens.

Figure 15 shows the simulated and experimental load–stroke curves during isothermal upsetting

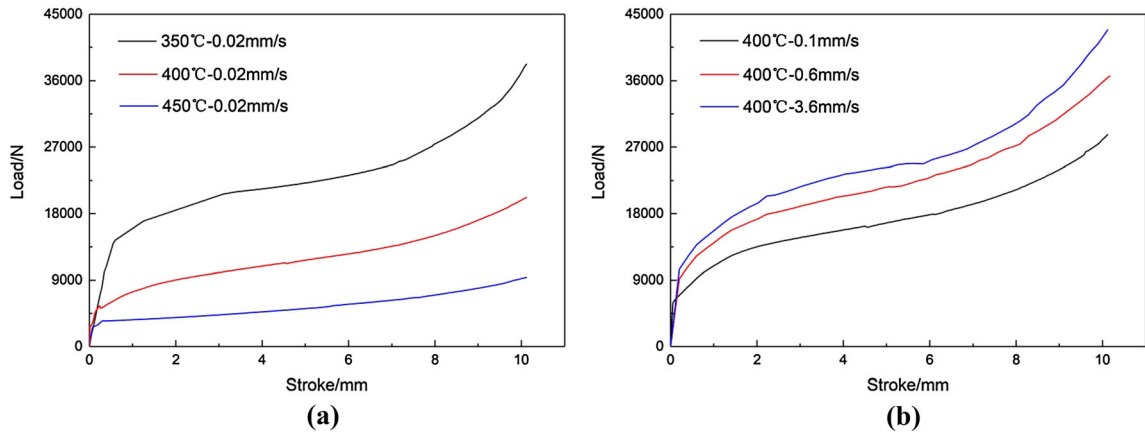


Fig. 13—The load–stroke curves of upsetting simulation: (a) at the same velocity and (b) temperature.

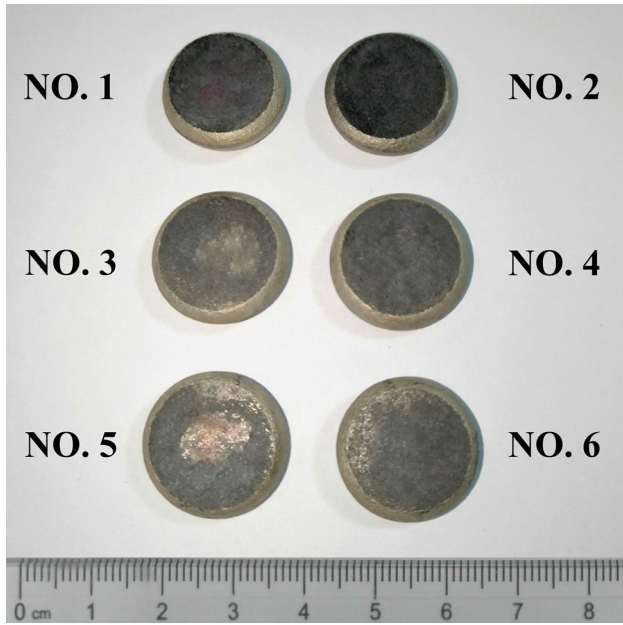


Fig. 14—The specimens after upsetting experiment under different process parameters.

Table V. Parameters Used for the Simulation of PSF

Number	Temperature (°C)	Velocity (mm/s)	Stroke (mm)
1	410	0.3	6.32
2	430	0.3	6.32
3	450	0.3	6.32
4	450	0.6	6.32
5	450	2	6.32
6	450	5	6.32

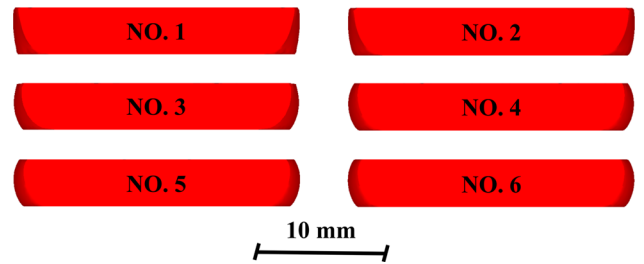


Fig. 16—The specimens after PSF simulation under different process parameters.

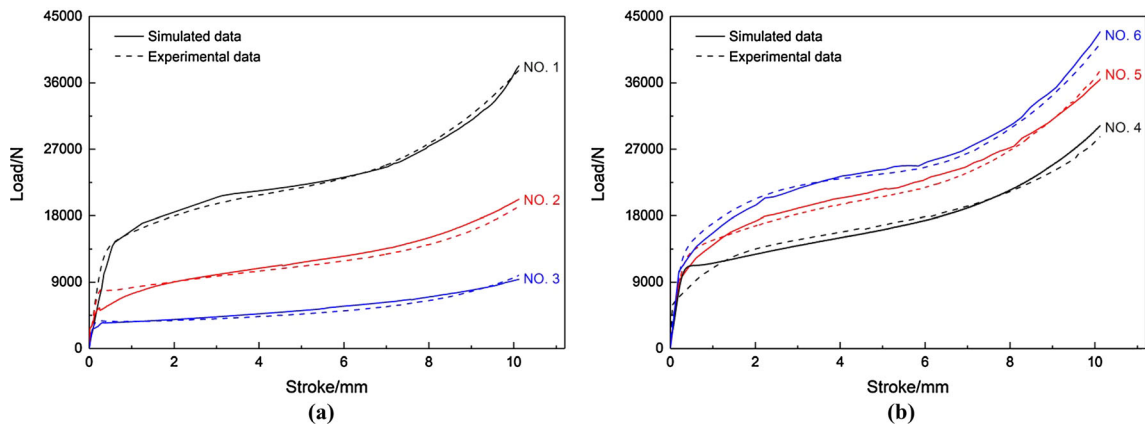


Fig. 15—Comparisons between simulation results and experimental results during the upsetting process: (a) at the same velocity and (b) temperature.

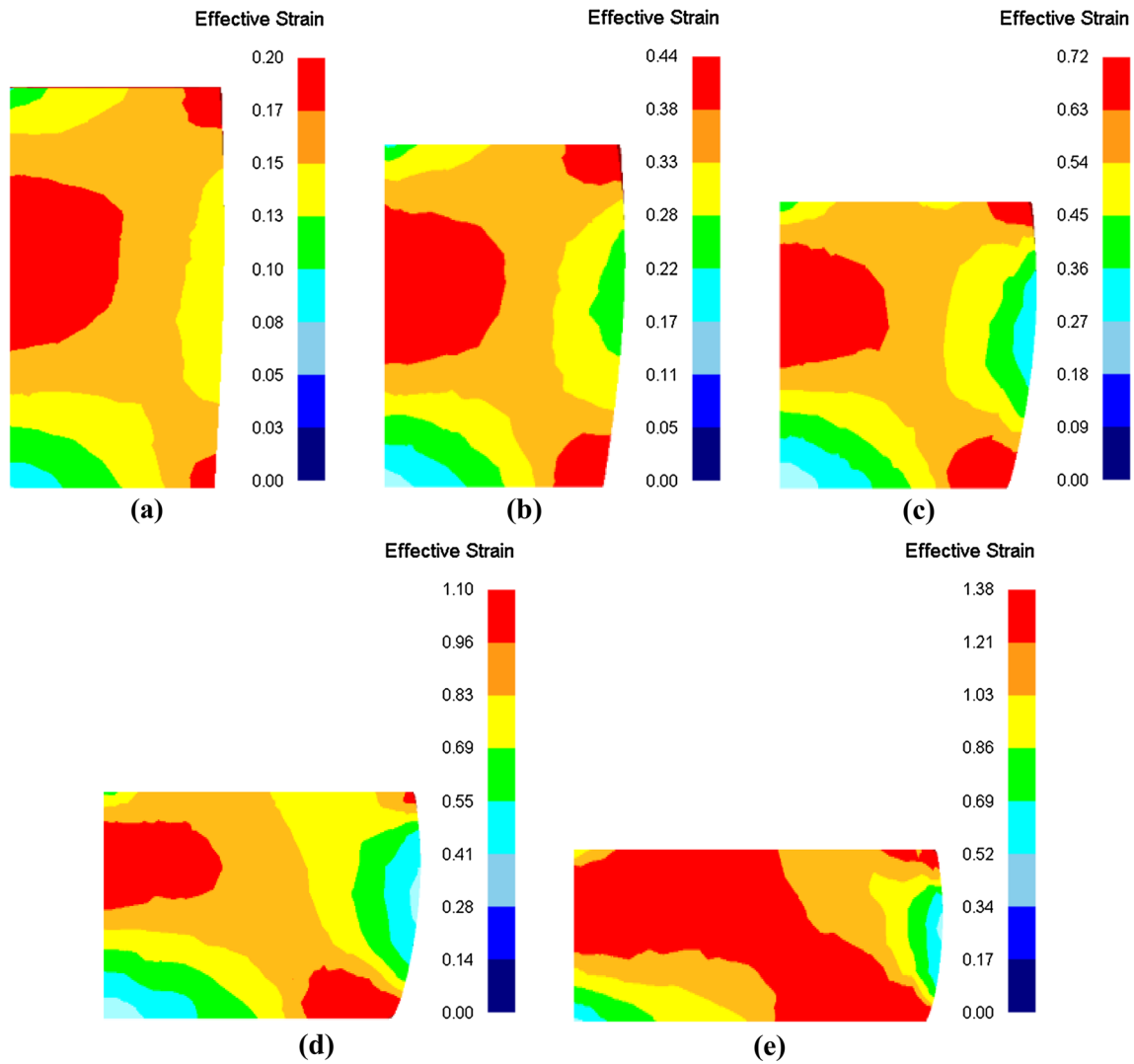


Fig. 17—Distributions of effective strain at different strokes during the PSF process: (a) 1.264 mm, (b) 2.528 mm, (c) 3.792 mm, (d) 5.056 mm, and (e) 6.32 mm.

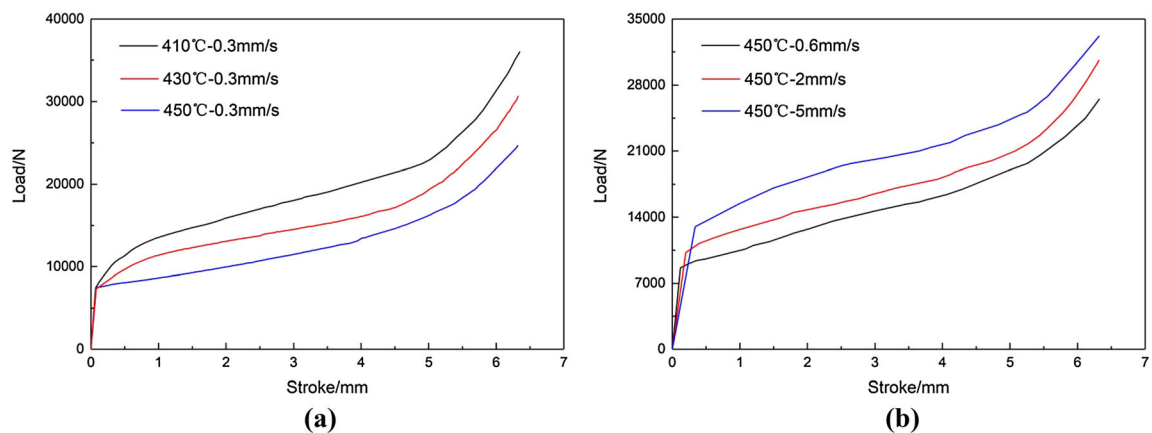


Fig. 18—The load–stroke curves of PSF simulation: (a) at the same velocity and (b) temperature.

specimen with VCS process. It can be noted that there are good agreements between the simulated and experimental results under different process

parameters, which proves that the new constitutive model of Mg alloys proposed in this paper is credible.

## B. Simulation Prediction and Experimental Verification of PSF

### 1. Simulation prediction of PSF

The load prediction of GW83 alloy during the PSF process under different deformation conditions was conducted. As listed in Table V, the first three groups are all in the same velocity, but belong to the different temperatures. The last three groups are opposite and have different velocities and same temperature.

The specimens after PSF simulation under different process parameters are shown in Figure 16. The shape of these samples is similar, and the length of these samples measured by the ruler below Figure 16 is about 22.1 mm. Figure 17 shows the effective strain distributions of the middle section of the sample at different strokes under the third parameter. Due to the symmetry, it can take half of the sample for analysis. It can be found from Figure 17(a) that the maximum effective strain occurs at the upper area of the center and two corner areas, and the contact areas between the billet and dies and the maximum outer edge area of the billet all have a small deformation. Then, the deformation zone with large strain expands gradually, as shown in Figures 17(b) through and (d). After deformation, the effective strain in a large area of the billet is more than 1.21, and the end of the specimen is drum-shaped due to the effect of friction (Figure 17(e)).

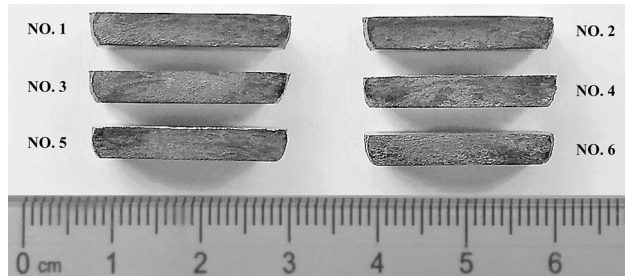


Fig. 19—The specimens after PSF experiment under different process parameters.

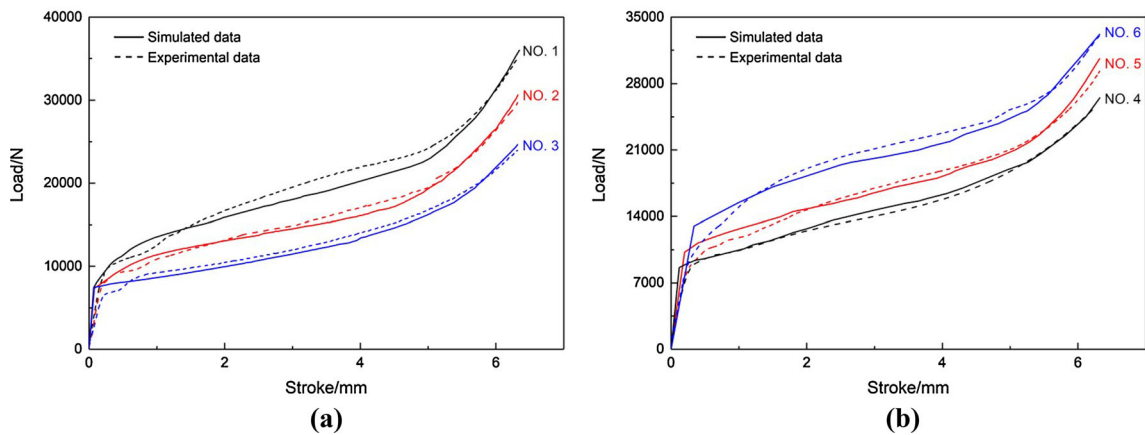


Fig. 20—Comparisons between simulation results and experimental results during the PSF process: (a) at the same velocity and (b) temperature.

Figure 18 is the simulation results of PSF, where the X-axis represents the stroke and the Y-axis represents the load. It can be observed that the change law of load during the PSF process is basically similar to that during the upsetting process, and the load decreases with the increase of temperature at the same velocity and increases with the increase of velocity at the same temperature.

### 2. Experimental verification of PSF

To validate the FE simulation results, the isothermal PSF experiments were performed under the process parameters that matched the FE simulation. The deformed specimens are shown in Figure 19, no macro-cracks exhibit on the surfaces of the samples, and the shape is roughly the same. The length of the samples after measurement is around 22.1 mm and identical with that of the simulated samples.

To clearly compare the load–stroke curves from simulation with that from experiment during the PSF process, Figure 20 was created. It can be seen that a good accordance between the simulated result and experimental result has been attained, which further confirms the accuracy of the new constitutive model.

## VI. CONCLUSIONS

- (1) Based on the isothermal thermal compression stress–strain curve of GW83 alloy, a new constitutive model was proposed by parameter regression. The model comprehensively reflects the effects of deformation temperature, strain, and strain rate on flow stress. The predicted values of the model are in good agreement with the experimental values.
- (2) The new constitutive model is proper not only for GW83 alloy, but also for AZ31B and ZK60 alloys. It is a constitutive model for thermal deformation of Mg alloys.
- (3) By integration of the new constitutive model with FE software, the isothermal upsetting specimen with VCS and PSF of GW83 alloy was simulated,

respectively. Combined with the experiment results, the accuracy of the new constitutive model was verified.

## ACKNOWLEDGMENTS

The authors gratefully acknowledge the supports of the National Key Research and Development Program of China (Grant No. 2016YFB0301103), the National Natural Science Foundation of China (Grant No. 51601112), and the Shanghai Rising-Star Program (Grant Nos. 16QB1402800 and 17QB1403000).

## REFERENCES

1. C. Meng, Z.K. Chen, H.N. Yang, G. Li, X.L. Wang, and H. Bao: *Metall. Mater. Trans. A*, 2018, vol. 49A, pp. 5192–5204.
2. D. Ghosh, O.T. Kingstedt, and G. Ravichaneran: *Metall. Mater. Trans. A*, 2017, vol. 48A, pp. 14–19.
3. H.C. Pan, F.H. Wang, M.L. Feng, L. Jin, J. Dong, and P.D. Wu: *Mater. Sci. Eng. A*, 2018, vol. 712, pp. 585–91.
4. H.L. Chen, J. Yang, H. Zhou, J. Moering, Z. Yin, Y.L. Gong, and K.Y. Zhao: *Metall. Mater. Trans. A*, 2017, vol. 48A, pp. 3961–70.
5. S.M. Fatemi, A. Zarei-Hanzaki, and J.M. Cabrera: *Metall. Mater. Trans. A*, 2017, vol. 48A, pp. 2563–73.
6. J.Q. Li, J. Liu, and Z.S. Cui: *Mater. Sci. Eng. A*, 2015, vol. 643, pp. 32–36.
7. M.Z. Bian, Z.R. Zeng, S.W. Xu, W.N. Tang, C.H.J. Davies, N. Birbilis, and J.F. Nie: *Metall. Mater. Trans. A*, 2016, vol. 47A, pp. 5709–13.
8. Y.Y. Dong, C.S. Zhang, X. Lu, C.X. Wang, and G.Q. Zhao: *J. Mater. Eng. Perform.*, 2016, vol. 25, pp. 2567–81.
9. Y.J. Wang, J. Peng, L.P. Zhong, and F.S. Pan: *J. Alloys Compd.*, 2016, vol. 681, pp. 455–70.
10. W.T. Jia, S. Xu, Q.C. Le, L. Fu, L.F. Ma, and Y. Tang: *Mater. Des.*, 2016, vol. 106, pp. 120–32.
11. Y.J. Qin, Q.L. Pan, Y.B. He, W.B. Li, X.Y. Liu, and X. Fan: *Mater. Sci. Eng. A*, 2010, vol. 527, pp. 2790–97.
12. H.T. Zhou, C.M. Liu, and M.A. Chen: *Mater. Sci. Technol.*, 2006, vol. 22, pp. 597–603.
13. Z.W. Cai, F.X. Chen, and J.Q. Guo: *J. Alloys Compd.*, 2015, vol. 648, pp. 215–22.
14. L.C. Tsao, Y.T. Huang, and K.H. Fan: *Mater. Des.*, 2014, vol. 53, pp. 865–69.
15. H. Takuda, T. Morishita, T. Kinoshita, and N. Shirakawa: *J. Mater. Process. Technol.*, 2005, vols. 164–165, pp. 1258–62.
16. J. Luan, C. Sun, X. Li, and Q. Zhang: *Mater. Sci. Technol.*, 2014, vol. 30, pp. 211–19.
17. M.S. Arun and U. Chakkingal: *Mater. Sci. Eng. A*, 2019, vol. 754, pp. 659–73.
18. H.T. Zhou, Q.B. Li, Z.K. Zhao, Z.C. Liu, S.F. Wen, and Q.D. Wang: *Mater. Sci. Eng. A*, 2010, vol. 527, pp. 2022–26.
19. G.Z. Quan, Y. Shi, C.T. Yu, and J. Zhou: *Mater. Res.*, 2013, vol. 16, pp. 785–91.
20. Q. Tang, M.Y. Zhou, L.L. Fan, Y.W.X. Zhang, G.F. Quan, and B. Liu: *Vacuum*, 2018, vol. 155, pp. 476–89.
21. Z.J. Wang, L.H. Qi, G. Wang, H.J. Li, and M.S. Dargusch: *Mech. Mater.*, 2016, vol. 102, pp. 90–96.
22. R.B. Mei, L. Bao, F. Huang, X. Zhang, X.W. Qi, and X.H. Liu: *Mech. Mater.*, 2018, vol. 125, pp. 110–20.
23. H. Yu, H.S. Yu, G.H. Min, S.S. Park, B.S. You, and Y.M. Kim: *Met. Mater. Int.*, 2013, vol. 19, pp. 651–65.
24. L. Li and X.M. Zhang: *Mater. Sci. Eng. A*, 2011, vol. 528, pp. 1396–1401.
25. Z.H. Zhou, Q.C. Fan, Z.H. Xia, A.G. Hao, W.H. Yang, W. Ji, and H.Q. Cao: *J. Mater. Sci. Technol.*, 2017, vol. 33, pp. 637–44.
26. R. Alizadeh, R. Mahmudi, O.A. Ruano, and A.H.W. Ngan: *Metall. Mater. Trans. A*, 2017, vol. 48A, pp. 5699–5709.
27. J.Q. Hao, J.S. Zhang, C.X. Xu, and K.B. Nie: *J. Alloys Compd.*, 2018, vol. 754, pp. 283–96.
28. Y. Sun, L.X. Hu, and J.S. Ren: *Mater. Charact.*, 2015, vol. 100, pp. 163–69.
29. S. He, C.S. Li, Z.Y. Huang, and J.J. Zheng: *J. Mater. Res.*, 2017, vol. 32, pp. 3831–41.
30. R. Bobbili and V. Madhu: *Mater. Sci. Eng. A*, 2017, vol. 700, pp. 82–91.
31. H.T. Zhou, X.Q. Zeng, Q.D. Wang, and W.J. Ding: *Acta Metall. Sin.*, 2004, vol. 17, pp. 155–60.
32. L.X. Xu, H.B. Wu, and B.S. Xie: *Mater. Sci. Technol.*, 2018, vol. 34, pp. 229–41.
33. Y. Bergstrom: *Mater. Sci. Eng.*, 1970, vol. 5, pp. 193–200.
34. A. Laasraoui and J.J. Jonas: *Metall. Trans. A*, 1991, vol. 22A, pp. 151–60.
35. A. Laasraoui and J.J. Jonas: *Metall. Trans. A*, 1991, vol. 22A, pp. 1545–58.
36. S. Serajzadeh and A.K. Taheri: *Mech. Res. Commun.*, 2003, vol. 30, pp. 87–93.
37. J. Liu, Z.S. Cui, and C.X. Li: *Comput. Mater. Sci.*, 2008, vol. 41, pp. 375–82.
38. C. Wang, J. Liu and Z.S. Cui: *J. Plast. Eng.*, vol. 18, pp. 22–27. (In Chinese).
39. L. Yuan, Z. Zhao, W.C. Shi, F.C. Xu, and D.B. Shan: *Int. J. Adv. Manuf. Technol.*, 2015, vol. 78, pp. 2037–47.
40. Y. Liu, C. Geng, Q.Q. Lin, Y.F. Xiao, J.R. Xu, and W. Kang: *J. Alloys Compd.*, 2017, vol. 713, pp. 212–21.
41. Z.P. Guan, M.W. Ren, P. Zhao, P.K. Ma, and Q.L. Wang: *Mater. Des.*, 2014, vol. 54, pp. 906–13.
42. H.T. Zhou, X.Q. Zeng, L.L. Liu, J. Dong, Q.D. Wang, W.J. Ding, and Y.P. Zhu: *Mater. Sci. Technol.*, 2004, vol. 20, pp. 1397–1402.
43. A.M.S. Hamouda: *J. Mater. Process. Technol.*, 2002, vol. 124, pp. 209–15.
44. J. Liu, Z.S. Cui, and C.X. Li: *J. Mater. Process. Technol.*, 2008, vol. 205, pp. 497–505.
45. A. Hadadzadeh, M.A. Wells, S.K. Shaha, H. Jahed, and B.W. Williams: *J. Alloys Compd.*, 2017, vol. 702, pp. 274–89.
46. H.J. Hu, H. Wang, Z.Y. Zhai, Y.Y. Li, J.Z. Fan, and Z.W. Qu: *Int. J. Adv. Manuf. Technol.*, 2015, vol. 76, pp. 1621–30.
47. S.S. Zhou, K.K. Deng, J.C. Li, K.B. Nie, F.J. Xu, H.F. Zhou, and J.F. Fan: *Mater. Des.*, 2014, vol. 64, pp. 177–84.

**Publisher's Note** Springer Nature remains neutral with regard to jurisdictional claims in published maps and institutional affiliations.